1 **Measurement report: Vertical and temporal variability of near-**
2 **surface ozone production rate and sensitivity in an urban area in Pearl**
3 **River Delta (PRD) region, China**

4 **Jun Zhou[1,2#], Chunsheng Zhang[3#], Aiming Liu[3], Bin Yuan[1,2*], Yan Wang[1,2],**
5 **Wenjie Wang[1,4], Jie-Ping Zhou[1,2], Yixin Hao[1,2], Xiao-Bing Li[1,2*], Xianjun He[1,2],**
6 **Xin Song[1,2], Yubin Chen[1,2], Suxia Yang[1,2], Shuchun Yang[1,2], Yanfeng Wu[1,2], Bin**
7 **Jiang[1,2], Shan Huang[1,2], Junwen Liu[1,2], Jipeng Qi[1,2], Minhui Deng[1,2], Yibo**
8 **Huangfu[1,2], Min Shao[1,2*]**

9 [1]Institute for Environmental and Climate Research, Jinan University, Guangzhou
10 511443, China

11 [2]Guangdong-Hongkong-Macau Joint Laboratory of Collaborative Innovation for
12 Environmental Quality, Guangzhou 511443, China

13 [3]Shenzhen National Climate Observatory, Shenzhen 518040, China

14 [4]Multiphase Chemistry Department, Max Planck Institute for Chemistry, Mainz 55128,
15 Germany

16 [#]These authors contribute equally to this work.

17 Correspondence: Bin Yuan (byuan@jnu.edu.cn), Xiao-Bing Li (lixiaobing@jnu.edu.
18 cn), Min Shao (mshao@jnu.edu.cn)

20 **Abstract**: Understanding the near-ground vertical and temporal photochemical O_3
21 formation mechanism is important to mitigate the O_3 pollution. Here, we measured the
22 vertical profiles of O_3 and its precursors at six different heights from 5-335 m using a
23 newly built vertical observation system in Pearl River Delta (PRD) region, China. The
24 net photochemical ozone production rate ($P(O_3)_{net}$) and O_3 formation sensitivities at
25 various heights were diagnosed using an observation-based model coupled with the
26 Master Chemical Mechanism (MCM v3.3.1). Moreover, for the assessment of model
27 performance and the causative factors behind O_3 pollution episodes, the net
28 photochemical ozone production rate ($P(O_3)_{net}$) was measured at 5 m ground level
29 utilizing a custom-built detection system. In total three O_3 pollution episodes and two
30 non-episodes were captured. The identified O_3 pollution episodes were found to be
31 jointly influenced by both photochemical production and physical transport, with local
32 photochemical reactions play a dominate role. The high index of agreement (IOA)
33 calculated from comparing the modelled and measured $P(O_3)_{net}$ values indicated the

34   rationality to investigate the vertical and temporal variability of O_3 formation

35   mechanism using modelling results. However, the measured $P(O_3)_{net}$ values were

36   generally higher than the modelled $P(O_3)_{net}$ values, particularly under high NOx

37   conditions, which may indicate a potential underestimation of total RO_2 by the model.

38   Throughout the measurement period, the contribution of different reaction pathways to

39   O_3 production remained consistent across various heights, with HO_2+NO as the major

40   O_3 production pathway, followed by RO_2+NO. We saw $P(O_3)_{net}$ decreased with the

41   increase of the measurement height, primarily attributed to the decreased O_3 precursors

42   anthropogenic organic compounds (AVOC) and oxygenated volatile organic

43   compounds (OVOC). O_3 formation regimes were similar at different heights during

44   both episodes and non-episodes, which was located either in volatile organic

45   compounds (VOCs) sensitive regime or in transition regime and more sensitive to

46   VOCs. Diurnally, photochemical O_3 formation typically remained in the VOCs

47   sensitive regime during the morning and noon time, but in the transitional regime and

48   more sensitive to VOCs in the afternoon at around 16:00 LT. The vertical and temporal

49   O_3 formation are most sensitive to AVOC and OVOC, which suggests that targeting

50   VOCs, especially AVOC and OVOC, for control measures is more practical and

51   feasible at the observation site. The vertical temporal analysis of O_3 formation

52   mechanisms near the ground surface in this study provides critical foundational

53   knowledge for formulating effective short-term emergency and long-term strategies to

54   combat O_3 pollution in the PRD region of China.

1. Introduction

56   Tropospheric ozone (O_3), which have adverse effects on ecosystems, climate change,

57   and human health (Fiore et al., 2009; Anenberg Susan et al., 2012; Seinfeld, 2016), has

58   become an important factor resulting severe regional air pollution in China (Zhu et al.,

59   2020). Tropospheric O_3 mainly comes from the external transport from the stratosphere

60   and the photochemical reactions of O_3 precursors, involving volatile organic

61   compounds (VOCs) and nitrogen oxides (NOx=NO+NO_2), and the ozone-precursor

62   relationship can be split into a "NOx-limited" or "VOC-limited" or "mixed-sensitive"

63   regime (Seinfeld and Pandis, 2016; Sillman S., 1999). Local O_3 concentrations can be

64   further affected by meteorological conditions and regional transport of O_3 and O_3

65   precursors (Gong and Liao, 2019; Chang et al., 2019). The Pearl River Delta (PRD) is

66   one of the most rapid economic development and urbanization area in China, which is

67   suffering from severe ground-level O_3 pollution (Lu et al., 2018; Yang et al., 2019).
68   Currently, the relationship between tropospheric ozone pollution and its precursors and
69   meteorological elements in PRD region have been analysed by many scholars (Mao et
70   al., 2022; Li et al., 2022a), which have greatly improved our understanding of the O_3
71   sources and formation processes in PRD region. However, the O_3 distribution is highly
72   variable at different altitudes (Wang et al., 2021), there was a vertical difference in
73   VOCs concentration and sources, and ozone formation sensitivity (Liu et al., 2023;
74   Tang et al., 2017). Using only one height's data for understanding the photochemical
75   reactions in the planetary boundary layer is of great limitation. Thus, diagnosing the O_3
76   formation mechanism at different heights is essential to achieve effective control of O_3
77   pollution.

78   Currently, high time resolution and real-time response remote sensing (for example,
79   lidar and optical absorption spectroscopy) has been utilized for measuring the vertical
80   distribution of O_3 (Luo et al., 2020a; Wang et al., 2021), however, the in situ
81   measurements of VOCs at different heights are mainly depends on the offline method
82   combined with different techniques, such as aircraft, tethered balloon, high buildings
83   and towers, unmanned aerial vehicles (UAVs or drones), satellite, etc. (Klein et al.,
84   2019; Li et al., 2022b; Geng et al., 2020; Benish et al., 2020; Li et al., 2021; Wang et
85   al., 2019). Owing to the low time resolution of these monitoring techniques, it is
86   difficult to achieve continuous vertical coverage of VOCs and NOx measurements, the
87   vertical distribution structure of VOCs is still unclear, thus largely hindered our in-
88   depth understanding of the vertical and temporal regional ozone formation mechanism.

89   To fill the gaps in the existing studies, we utilized a newly built vertical
90   observation system based on the Shenzhen Meteorological Gradient Tower (SZMGT)
91   (Li et al., 2023). This system measured the vertical profiles of O_3 and its precursors at
92   six different heights from 5-335 m. To diagnose the $P(O_3)_{net}$ and O_3 formation
93   sensitivities across various heights, we employed an observation-based model coupled
94   with the Master Chemical Mechanism (MCM v3.3.1). Additionally, we employed a
95   novel net photochemical ozone production rate ($P(O_3)_{net}$, NPOPR) detection system to
96   measure the $P(O_3)_{net}$ at the 5 m ground level to explore potential reasons for O_3
97   pollution episodes (Hao et al., 2023), i.e., examine the contribution of chemical and
98   physical processes to changes in O_3 concentration. Comparisons between the directly

99   measured $P(O_3)_{net}$ results and the model-derived data enabled us to evaluate the

100 simulation accuracy and explore potential reasons for discrepancies of the OBM-MCM

101 model concerning photochemical O_3 formation. Based on these results, we extensively

102 discussed the vertical and temporal variability in $P(O_3)_{net}$ and O_3 formation sensitivity,

103 while acknowledging potential biases associated modelling. The findings of this study

104 offer a new benchmark for understanding the vertical profile of photochemical O_3

105 formation mechanism, aiding in the identification of the primary driver of ground-level

106 O_3 pollution. This identification is crucial as it can provide essential theoretical support

107 for developing short-term effective emergency and long-term control measures

108 targeting O_3 in PRD region in China.

109 **2.   Materials and Methods**
110 **2.1 Sampling site**

111 Field measurements were conducted at Shenzhen Meteorological Gradient Tower

112 (SZMGT) (22.65° N,113.89° E) from 13 November to 10 December, 2021. SZMGT is

113 currently the tallest mast tower in Aisa and the second tallest of this kind in the world,

114 which is located in the Tiegang Reservior Water Reserve at Bao'an District of Shenzhen,

115 in Pearl River Delta (PRD) region of China. High density of vegetation, reservoir

116 features, low-rise buildings, and hills/mountains are surrounded (Luo et al., 2020b).

117 **2.2 Instrumentation**
118 **2.2.1   The vertical sampling system**

119   A tower-based observation system for traces gases was used to sample the O_3 and O_3

120 precursors at 6 heights, including 5, 40, 70, 120, 220, and 335 m above the ground

121 during the campaign. This system was established using long perfluoroalkoxy alkane

122 (PFA) tubing. The impacts of long tubing on measurements of various of trace gases,

123 including O_3, NOx, and a set of organic compounds were systematically investigated

124 using a combination of laboratory tests, field experiments, and modelling techniques.

125 Field observations proved that this observation system is suitable for analyzing spatio-

126 temporal variations of atmospheric trace gases, with many trace gases could be well

127 measured. More details about the establish and the characterization about this

128 observation system are described elsewhere (Li et al., 2023).

129 **2.2.2 $P(O_3)_{net}$ measurement**

130 During the campaign, the $P(O_3)_{net}$ at the 5 m ground level was measured using the self-

131 developed NPOPR detection system, which was built based on the dual-channel

132 reaction chambers technique. The improvement, characterization, and the

133 photochemical O_3 formation mechanism in the reaction and reference chambers of the

134 NPOPR detection system are described in our previous study (Hao et al., 2023). Briefly,

135 the NPOPR detection system consists of reaction and reference chambers with the same

136 geometry and made of quartz glass, the length and inner diameter of the quartz glass

137 cylinder are 700 mm and 190.5 mm, respectively, which resulted in an inner volume of

138 ~ 20 L. The outer surface of the reference chamber was covered with an Ultem film

139 (SH2CLAR, 3 M, Japan) for ultraviolet (UV) protection, which can block sunlight with

140 wavelengths < 390 nm thus preventing photochemical reactions inside. During the

141 experiment, both the reaction and reference chambers were placed outdoors and directly

142 exposed to sunlight to simulate real ambient photochemical reactions. Ambient air was

143 introduced into the reaction and reference chambers at the same flow rate, and a Teflon

144 filter was mounted before the chamber inlet to remove fine particles. To correct the

145 effects of fresh NO titration to O_3, we use O_x ($=O_3+NO_2$) instead of O_3 to quantify the

146 O_3 generated by photochemical reactions (Pan et al., 2015; Tan et al., 2018). A stream

147 of air from the two chambers was alternately introduced into an NO-reaction chamber

148 every 2 min to convert O_3 in the air to NO_2 in the presence of high concentrations of

149 NO ($O_3+NO=NO_2$), and the Ox concentrations from the outlet NO-reaction chamber,

150 i.e., the total NO_2 concentrations including the inherent NO_2 in the ambient and that

151 converted from O_3, were measured by a Cavity Attenuated Phase Shift (CAPS) NO_2

152 Monitor (Aerodyne research, Inc., Billerica MA, USA) to avoid other nitrogen oxide

153 interferences to the NO_2 measurement (such as alkyl nitrates, peroxyacyl nitrates,

154 peroxynitric acid, nitrogen pentoxide, etc.). $P(O_3)_{net}$ was obtained by dividing the

155 difference between the Ox concentrations in the reaction and reference chambers (ΔOx)

156 by the mean residence time of air in the reaction chamber $\langle\tau\rangle$:

157 $$P(O_3)_{net} = P(O_X)_{net} = \frac{\Delta O_X}{\tau} = \frac{[O_X]_{reaction} - [O_X]_{reference}}{\tau} \qquad (1)$$

158   A schematic of the NPOPR detection system is shown in Fig. S1. The mean

159 residence time is 0.063 h at the air flow rate of 5 L min^{-1}, which was obtained by

160 introducing a short pulse of NO_2 gas (obtained by mixing 0.2 L min^{-1} of 2.08 ppmv

161 NO_2 standard gas with 5.2 L min^{-1} ultrapure air) into the reaction chamber at $\tau = 0$, the

162 time profile of NO_2 mixing ratios ($C(\tau)$) at the exit of the chamber was measured using

163   the CAPS-NO_2 monitor. The pulse width of the introduced NO_2 gas was approximately

164   20 s and sufficiently shorter than $\langle\tau\rangle$. $C(\tau)$ was then normalized and converted to a

165   probability density function ($E(\tau)$) (Sadanaga et al., 2017):

166    $$E\langle\tau\rangle = \frac{C(\tau)}{\int_0^\infty C(\tau)\,d\tau}$$ (2)

167   The expected $\langle\tau\rangle$ value was then calculated using Eq. (3):

168    $$\langle\tau\rangle = \int_0^\infty \tau E\langle\tau\rangle d\tau = \int_0^\infty \frac{\tau C(\tau)}{\int_0^\infty C(\tau)\,d\tau}\,d\tau$$ (3)

169   We further quantified and corrected the wall losses of Ox and the light-enhanced

170   loss of O_3 ($d[O_3]$) in the reaction and reference chambers during daytime:

171    $$\gamma = \frac{d[O_3]\times D}{\omega\times[O_3]\times\tau}$$ (4)

172   where γ is the light-enhanced loss coefficient of O_3, $[O_3]$ represents the difference

173   between the O_3 mixing ratios at the inlet and outlet of the reaction and reference

174   chambers, D is the diameter of the chambers, ω is the average velocity of O_3 molecules,

175    $[O_3]$ is the injected O_3 mixing ratio at the inlet of the reaction and reference chambers,

176   and τ is the average residence time of the air in the reaction and reference chambers. γ

177   is calculated as a function of $J(O^1D)$. The relationship of γ with $J(O^1D)$ is obtained from

178   the laboratory calibration tests in our previous study (Hao et al., 2013).

179   The limit of detection (LOD) of the NPOPR detection system is 2.3 ppbv h^{-1} at the

180   sampling air flow rate of 5 L min^{-1}, which is obtained as three times the measurement

181   error of $P(O_3)_{net}$. The measurement error of $P(O_3)_{net}$ is mainly determined by the

182   measurement precision of Ox by the CAPS NO_2 monitor, the light-enhanced loss of O_3,

183   the chamber Ox losses, and the residence time, as demonstrated in our previous study

184   (Hao et al., 2013). The measurement accuracy of NPOPR detection system is

185   determined as 13.9 %, which is the maximum systematic error caused by the

186   photochemical O_3 productions in the reference chamber. As the UV protection Ultem

187   film covered on the reference chamber can only filtered out the sunlight with

188   wavelengths < 390 nm, the photochemical O_3 productions at the sunlight wavelength

189   between 390 nm and 790 nm still exists in the reference chamber. The photochemical

190   reactions in the reaction and reference chambers have been thoroughly studied in our

191   previous studies (Hao et al., 2023), and we found that while the modelled $P(O_3)_{net}$ in

192   the reaction chamber is similar with that modelled in the ambient air, the modelled

193    $P(O_3)_{net}$ in the reference chamber accounted 0-13.9% of that in the reaction chamber.

194   Therefore, we corrected the measured $P(O_3)_{net}$ using the quantified $P(O_3)_{net}$ in the

195   reference chamber.

2.2.3 VOCs measurement

197   VOCs were measured using a high-resolution proton transfer reaction time-of-flight

198   mass spectrometry (PTR-TOF-MS, Ionicon Analytik, Austria) (Wang et al., 2020a; Wu

199   et al., 2020) and an off-line gas chromatography mass spectrometry flame ionization

200   detector (GC-MS-FID) (Wuhan Tianlong, Co. Ltd, China) (Yuan et al., 2012). The

201   concentrations of oxygenated VOCs (OVOC), including formaldehyde (HCHO) and

202   acetaldehyde (CH_3CHO), were measured via PTR-TOF-MS, and the non-methane

203   hydrocarbons (NMHC) were measured via GC-MS-FID. PTR-TOF-MS was running

204   with both hydronium ion (H_3O^+) (Yuan et al., 2017; Wu et al., 2020) and nitric oxide

205   ion (NO^+) (Wang et al., 2020) modes. The measurement error of PTR-TOF-MS was

206   lower than 20%, more details of the PTR-TOF-MS technique can be found in our

207   previous publication (Yuan et al., 2017). The H_3O^+ and NO^+ modes were automatically

208   switched with 20 min H_3O^+ mode and 10 min NO^+ mode. The background signal of

209   each mode was determined at the last 2 min, by automatically switching ambient

210   measurement to a custom-built platinum catalytic converter heated to 365 ºC.

211   Eventually, we only used VOCs measured during H_3O^+ mode, which was operated with

212   a drift tube pressure of 3.8 mbar, temperature of 120 ºC, and voltage of 760 V, 3035

213   ions with m/z up to 510 were obtained at time resolutions of 10 s. A gas standard with

214   35 VOC species was used for calibrations of the PTR-ToF-MS once per day. Raw data

215   from PTR-TOF-MS were analyzed using Tofware software (Tofwerk AG, v3.0.3). Due

216   to the humidity dependencies of various VOCs signals of the PTR-ToF-MS observed

217   in laboratory study, we have determined their humidity-dependence curves, such as

218   formaldehyde, benzene, methanol, ethanol, and furan (Wu et al., 2020). During the data

219   analysis, we removed the impacts of ambient humidity change on the measured signals

220   of the PTR-ToF-MS according to these humidity-dependence curves.

2.2.4 Other parameters

222   The photolysis frequencies of different species were measured using the actinic flux

223   spectrometer (PFS-100, Focused Photonics Inc, China). O_3 and NO_X concentrations

224   were measured by a 2B O_3 monitor based on dual-channel UV-absorption (Model 205,

225   2B Technologies, USA) and a chemiluminescence NOx monitor (Model 42i, Thermo

226   Fisher Scientific, USA), respectively. Temperature (T), relative humidity (RH), and

227   pressure (P) were measured by a portable weather station (Met Pak, Gill Instruments

228   Ltd, UK).

229   **2.3 Data analysis**
230   **2.3.1   Observation-based chemical box model**

231   We investigated the detailed photochemical O_3 formation mechanism during the

232   observation period based on the field observed data. The specific tropospheric O_3

233   photochemical formation process is the photolysis of NO_2 at 424 nm, simultaneously,

234   there are RO_X (RO_X=OH+HO_2 +RO_2) radical recycles provide HO_2 and RO_2 to oxidize

235   NO to NO_2 resulting in the accumulation of O_3 (Shen et al., 2021; Cazorla and Brune,

236   2010; Sadanaga et al., 2017), therefore, the ROx radicals and the O_3, OH, NO_3 oxidants

237   play important roles in photochemical O_3 formation. A zero-dimensional box model

238   based on the Framework for 0-D Atmospheric Modelling (F0AM) v3.2 (Wolfe et al.,

239   2016) coupled with the MCM v3.3.1 was used to simulate the $P(O_3)_{net}$. MCM v3.1.1

240   contains a total of 143 VOCs, more than 6700 species, involving more than 17000

241   reactions (Jenkin et al., 2015). Through the constraint T, RH, P, organic and inorganic

242   substances in gases to simulate $P(O_3)_{net}$, including 12 OVOCs (methanol, ethanol,

243   formaldehyde, acetaldehyde, acrolein, acetone, hydroxyacetone, phenol, *m*-cresol,

244   methyl vinyl ketone, methacrylaldehyde, methyl ethyl ketone), 47 non-methane

245   hydrocarbons (toluene, benzene, isoprene, styrene, etc.), conventional pollutants (O_3,

246   NO, NO_2, and CO), and photolysis rate values ($J(O^1D)$, $J(NO_2)$, $J(H_2O_2)$, $J(HONO)$,

247    $J(HCHO\_M)$, $J(HCHO\_R)$, $J(NO_3\_M)$, $J(NO_3\_R)$, etc.). $P(O_3)_{net}$ can be expressed by

248   the difference between ozone production rate ($P(O_3)$) and ozone destruction rate

249   ($D(O_3)$), $P(O_3)$, and $D(O_3)$ can be calculated as Eq. (5)-(6).

250    $P(O_3) = k_{HO_2+NO}[HO_2][NO] + \sum_i k_{RO_{2,i}+NO}[RO_{2i}][NO]\varphi_i$ (5)

251    $D(O_3) = k_{O(^1D)+H_2O}[O(^1D)][H_2O] + k_{OH+O_3}[OH][O_3] + k_{HO_2+O_3}[HO_2][O_3]$

252    $+k_{O_3+alkenes}[O_3][alkenes] + k_{OH+NO_2}[OH][NO_2] + k_{RO_{2,i}+NO_2}[RO_{2i}][NO_2]$ (6)

253   where k_{M+N} represents the bimolecular reaction rate constant of M and N, the subscript

254   'i' refers to different types of RO_2, and φ_i is the yield of NO_2 of the reaction RO_{2i}+NO.

255   The relevant reaction rates of $P(O_3)$ and $D(O_3)$ and the mean measured concentrations

256   of each VOC category at 5 m ground during O_3 episodes and non-episodes used in the

257   model are listed in Tables S1 and S2. A "spin up" for 3 days before the modelling days

258   was applied in the model to get the radical intermediates steady.

259   **2.3.2   Derive contribution of chemical and physical processes to O_3 changes**
260   **on the ground level**

261   It is known that chemical and physical processes jointly influence the O_3 concentration

262   changes near the ground surface (Xue et al., 2014; Tan et al., 2019). The direct

263   measurement of $P(O_3)_{net}$ gave us a chance to identify the contribution of chemical and

264   physical processes to the variation of observed O_3 concentrations using the following

265   equation:

266
$$\frac{dO_X}{dt} = P(O_X)_{net} + R(O_X)_{trans} \tag{7}$$

267   Where $\frac{dO_X}{dt}$ is the change rate of the observed O_x mixing ratio change (ppbv h^{-1}),

268     $P(O_3)_{net}$ denotes the net photochemical O_3 production rate (ppbv h^{-1}), which was equal

269   to $P(O_3)_{net}$ and measured directly by NPOPR system, $R(O_X)_{trans}$ represents O_3 mixing

270   ratio change due to the physical transportation (ppbv h^{-1}), including the horizontal and

271   vertical transport, dry deposition and the atmospheric mixing (Liu et al., 2022). To

272   correct the effects of NO titration to O_3, we have replaced O_3 with O_x (=O_3+NO_2) during

273   the calculation in this study (Pan et al., 2015).

274   **2.3.3   Model performance**

275   In order to judge the reliability of the model simulation, we calculated the index of

276   agreement (IOA) based on the measured and modelled $P(O_3)_{net}$ at 5 m above the ground

277   level using the following equation (Liu et al., 2019):

278
$$IOA = 1 - \frac{\sum_{i=1}^{n}(O_i - S_i)^2}{\sum_{i=1}^{n}(|O_i - \bar{O}| - |S_i - \bar{O}|)^2} \tag{8}$$

279   Where S_i and O_i represents the simulated and observed $P(O_3)_{net}$ or O_3 values at the

280   same time, respectively, $\bar{O}$ is the averaged observed value, and n is the data number.

281   Further, we also judged the model simulation performance using statistical measures,

282   including the correlation coefficient, normalized mean bias (NMB) and normalized

283   mean error (NME), which are defined as:

$$NMB = \frac{\sum_{i=1}^{n}(S_i - O_i)}{\sum_{i=1}^{n} O_i} \cdot 100 \% \tag{9}$$

$$NME = \frac{\sum_{i=1}^{n}|S_i - O_i|}{\sum_{i=1}^{n} O_i} \cdot 100 \% \tag{10}$$

Where S_i and O_i have the same meaning as Eq. (8), and n is the total number of such data pairs of interest. The results will be discussed in Sect. 3.2.2.

2.3.4 OH reactivity

In order to investigated the influence of the photochemical reactions of different VOCs to photochemical O_3 formation, we calculated the OH reactivities of different VOCs, i.e., the sum of concentrations of OH reactants multiplied by their reaction rate coefficients, as shown below:

$$k_{OH} = k_i \times [VOCs]_i \tag{11}$$

where k_{OH} represents the total OH reactivity of a group of VOCs species, k_i represents the rate constants between OH radicals and different VOCs species i, $[VOCs]_i$ represent the concentration of species i. In this study, we summarized the OH reactivities of different kinds of VOCs groups together to investigated their influence to the gradient $P(O_3)_{net}$ change with heights in Sect. 3.2.3.

2.3.5 Ozone formation regime

The sensitivity of photochemical O_3 production to its precursors was diagnosed by calculating the relative incremental reactivity (RIR) using the OBM-MCM model. RIR is defined as the O_3 photochemical production percent change due to per percent change in its single precursor/precursor group concentrations (Cardelino and Chameides, 1995). Therefore, the RIR for precursor (group) X can be expressed as:

$$RIR = \frac{\Delta P(O_3)/P(O_3)}{\Delta X/X} \tag{12}$$

where the $\Delta X/X$ represent the percent change in different O_3 precursor or precursor groups. We classified the measured VOCs into anthropogenic organic compounds (AVOC), biogenic organic compounds (BVOC), and OVOC group, and investigated the O_3 formation sensitivity to these different types of VOCs.

3. Results and discussions

3.1 Vertical and temporal profile of ozone and its precursors

3.1.1 Ozone and its precursors at 5 m ground level

Figure 1 shows the time series of the major trace gases, photolysis rate constants, and meteorological parameters at 5 m ground-level during the observation period at SZMGT. During the 1-month field observation period, in total 3 O_3 pollution episodes (referred to episodes hereafter) and 2 non-O_3 pollution episodes (referred to non-episodes hereafter) were captured, the O_3 pollution episodes were defined as the days during which the hourly average ozone concentration on the ground-level (5 m) exceed the Grade II standard (102 ppbv, GB 3095-2012, China; Ambient air quality standards, 2012), the rest days were defined as non-episodes. Episode days (marked as gray columns in Fig. 1) including 13-18 November (episode I), 26 November (episode II), and 7-9 December (episode III), while the non-episode days including 22-25 November (non-episode I), 26-27 and 30 November (non-episode II). The corresponding daytime mean values (6:00-18:00 LT) during all episode days and non-episode days are shown in Table 1. During the daytime of episode days (episodes I, II, and III), the mean concentrations of O_3 were 70.1±28.6, 59.5±32.4, and 71.3±31.0, respectively. The mean T and RH were 22.3±2.5 °C and 56.2±14.5 % for episode I, 20.4±3.2 °C and 52.2±16.7 % for episode II, and 20.6±3.4 °C and 58.2±17.2 % for episode III. During non-episode days, the mean concentrations of O_3 were 45.3±16.2 and 63.7±21.3 ppbv for non-episode I and II, respectively. The corresponding mean T and RH were 18.4±4.3 °C and 69.5±15.4 % for non-episode I, and 21.3±2.7 °C and 51.8 ±13.7 % for non-episode II. These observations indicate that the T and RH during episode days were not statistically different from those during non-episode days. This phenomenon contrasts with previous studies in PRD area, where O_3 pollution episodes were generally associated with high T and low RH (Mousavinezhad et al., 2021; Hong et al., 2022).
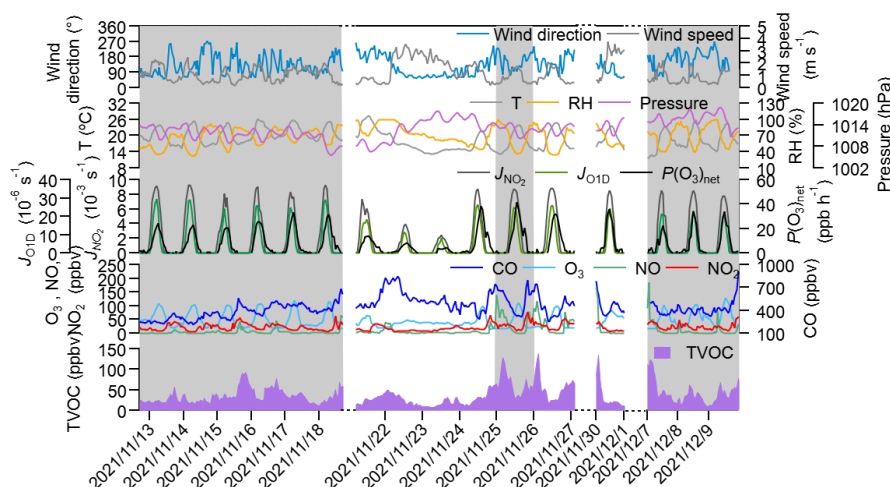
Figure 1. Time series of major trace gases, photolysis rate constants, and meteorological parameters at 5 m ground level during the observation period. The gray columns show the typical O_3 episodes that occurred.

Table 1. Daytime major trace gases concentrations (units: ppbv), $P(O_3)_{net}$ (units: ppbv h^{-1}), and meteorological parameters during different episodes and non-episodes during the observation period (from 13 November to 9 December 2021) at SZMGT.

Parameters	Mean±SD				
	Episode I	Episode II	Episode III	Non-episode I	Non-episode II
O_3	70.1±28.6	59.5±32.4	71.3±31.0	45.3±16.2	63.7±21.3
TVOC	29.6±10.6	53.8±21.7	42.9±11.5	23.3±8.6	26.8±11.1
CO	344.9±85.1	408.8±85.4	397.2±42.1	508.5±117.2	383.4±74.6
NO	2.3±2.6	13.1±17.4	6.6±13.8	2.9±2.0	6.8±13.1
NO_2	15.6±7.5	22.3±10.2	20.0±8.3	14.1±6.8	15.4±8.8
OFP (g m^{-3})	5.1E-4± 7.5E-5	1.0E-3± 2.0E-4	7.2E-4± 8.3E-5	4.1E-4± 5.6E-5	4.7E-4± 7.8E-5
$P(O_3)_{net}$ * (ppbv h^{-1})	14.3±10.7	21.5±14.9	14.6±11.9	5.6±4.6	18.9±13.9
T (℃)	22.3±2.5	20.4±3.2	20.6±3.4	18.4±4.3	21.3±2.7
RH (%)	56.2±14.5	52.2±16.7	58.2±17.2	69.5±15.4	51.8±13.7
wind speed (m s^{-1})	1.3±0.5	1.2±0.4	1.1±0.5	1.8±0.9	2.1±0.9
wind direction (°)	115.5±48.7	128.6±35.3	144.8±57.1	115.0±57.6	115.3±36.2

* All values here were calculated as the mean average values during daytime (6:00-18:00 LT).

The mean concentrations of O_3 precursors, including CO, NO, NO_2, and TVOC, were not statistically different between episodes and non-episodes. This suggests that

347   their concentrations during O_3 pollution episodes can vary, being either higher or lower

348   than those observed during non-episodes (as shown in Table 1). We further compared

349   daytime mean O_3 formation potential (OFP) and measured $P(O_3)_{net}$ during episodes and

350   non-episodes, and found that daytime average OFP and $P(O_3)_{net}$ on episode days were

351   also not statistically different with those during non-episode days, considering a range

352   within one standard deviation. These findings indicate that the O_3 pollution episodes

353   stem from either substantially elevated local photochemical O_3 formation (i.e., episode

354   II), or the accumulation of O_3 formed by moderate local photochemical O_3 formation

355   under stable weather conditions (i.e., episodes I and II). Notably, when local

356   photochemical reactions contribute intensely to the formation of O_3, favorable weather

357   conditions facilitating O_3 outflow diminish the likelihood of O_3 pollution occurrences

358   (i.e., non-episode II). In summary, O_3 pollution episodes are jointly affected by the

359   photochemical reactions and physical transport processes, which we will discuss further

360   in Sect. 3.2.1.

361   **3.1.2   Vertical profiles of ozone and its precursors at 5-335m level**

362   Figure 2 shows the contour plots illustrating the vertical profiles of O_3, NOx,

363   Ox(=O_3+NO_2), and TVOC. From Fig. 2, minimal vertical gradients exist in the

364   concentration of all species−O_3, NOx, Ox, and TVOC−due to the rapid vertical mixing

365   effects. However, distinct vertical gradients were observed during nighttime owing to

366   the stability of the nocturnal residual layer. Elevated concentrations of O_3 and Ox were

367   identified at higher altitudes, whereas higher NOx concentrations predominantly

368   occurred at ground level. We further elucidated the vertical distribution patterns of

369   different pollutants as well as the OFP of different VOCs groups during local daytime

370   (6:00-18:00 LT) and nighttime (19:00-5:00 LT) for both episodes and non-episodes, as

371   shown in Fig. 3.

372

373

374

375

376

377

378

379

380

381

382

383

384

385

386

387

388

389

390

391

392

393

394

395

396

397

398

399

400

401

402

403
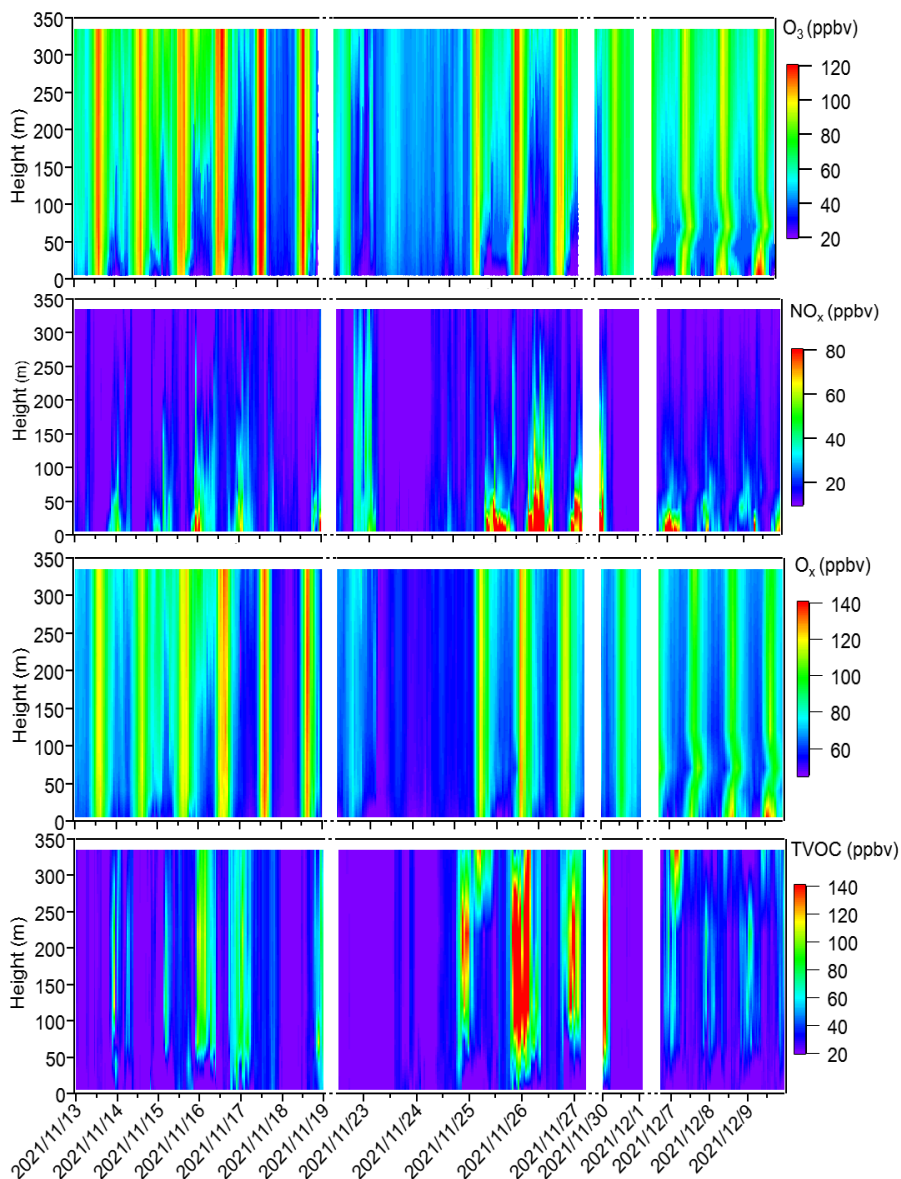
404

405 **Figure 2. Time series of vertical profiles for O₃, NOx, Ox, and TVOC during the observation**
406 **period. The contour plots are made using the measured values from six heights.**
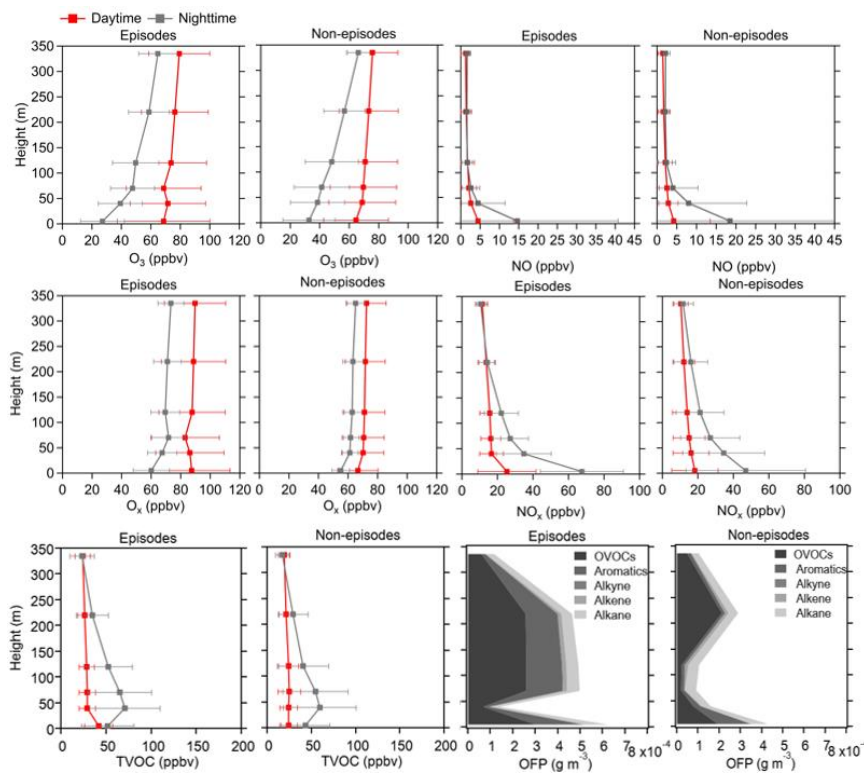
Figure 3. Average vertical profiles of O₃, NO, Ox, NOx, and TVOC during both daytime and nighttime, and OFP of different VOCs types during daytime at six heights (5, 40, 70, 120, 220, and 335 m), including episodes and non-episodes throughout the observation period. The error bars indicate the standard deviation calculated from the measured values during these periods.

The vertical profiles of averaged concentrations of various pollutants exhibit similar trends during both episodes and non-episodes, with O_3 showing an increasing trend from 5 m above ground level to 355 m, aligning with findings from previous studies (Zhang et al., 2019; Wang et al., 2021). Given that NOx has a significant titration effect on ozone, the lower O_3 concentration at ground level may be attributed to the increase in NOx concentration (Zhang et al., 2022) and also the dry deposition near the ground (Li et al., 2022b). NO and NOx showed an opposite trend compared to O_3. These two factors jointly effected the Ox changing trend with heights, and consequently, the gradients of Ox concentrations showed a weaker increasing trend from the 5 m ground

424 level to 355 m height compared to O_3. This observation demonstrated a more

425 pronounced NO titration effect at the 5 m ground level compared to the effect at 355 m

426 height. However, the TVOC showed variable trends with the increased height for

427 daytime and nighttime during episodes and non-episodes. During daytime, TVOC

428 initially decreased from 5 m to 40 m, and then continuously increased from 40 m to 355

429 m during episodes, while continuously slightly decreased from 5 m to 335 m during

430 non-episodes. During nighttime, TVOC concentrations first increased from 5 m to 40

431 m and then continuously decreased from 40 m to 335 m during both episodes and non-

432 episodes. We further plotted the OFP of different VOCs groups at various altitudes, and

433 found that the total OFP was highest at 5 m ground level and exhibited higher levels

434 during episodes compared to non-episode periods. Subsequently, there was a significant

435 decrease at 40 m height during both episodes and non-episodes. However, there was a

436 sharp increase observed at 70 m, 120 m, and 220 m during episodes, contrasting with a

437 gradual rise during non-episode periods, which eventually reach a peak at 220 m during

438 non-episodes. Besides, a consistent decrease of OFP from 220 m to 335 m was observed

439 during both episodes and non-episodes. The OFP was primarily attributed to OVOCs

440 at different altitudes throughout both episodes and non-episodes, followed by aromatics

441 and alkane during episodes and non-episodes, respectively.

442 **3.2 O_3 pollution episodes formation mechanism at near-ground surface**

443 In this section, we first explored the possible reason for O_3 pollution episodes on the 5

444 m ground level, i.e., identify the contribution of chemical and physical processes to O_3

445 concentration changes (Sect. 3.2.1), then checked the modelling performance and the

446 possible reason for the modelling bias in photochemical O_3 formation by comparing the

447 measured $P(O_3)_{net}$ with the modelled $P(O_3)_{net}$ (Sect. 3.2.2). To gain insights into the

448 photochemical O_3 formation mechanism at different heights and understand their role

449 in overall O_3 pollution, we further discussed the chemical budget of O_3 at different

450 heights (Sect. 3.2.3), the vertical and temporal variability of $P(O_3)_{net}$ and O_3 formation

451 regime (Sect. 3.2.4) , and their possible bias within the modelling approach (Sect. 3.2.5).

452 **3.2.1 Contribution of chemical and physical processes to O_3 changes on the**
453 **ground level**

454 As concluded in Sect. 3.3.1, O_3 pollution episodes may be jointly affected by the

455 photochemical reactions and physical transport. In order to identify the main reasons

456 for O_3 pollution on the ground level, we calculated the contribution of chemical and

457 physical processes to O_3 changes at 5 m ground level separately for all 3 episodes and

458 2 non-episodes. As the dry deposition are usually contribute a quite small portion and

459 can be negligible, the main contributor to physical processes is the vertical and

460 horizontal transport (Tan et al., 2019). Their hourly averages and diurnal variations are

461 shown in Figs. 4 and 5, respectively.
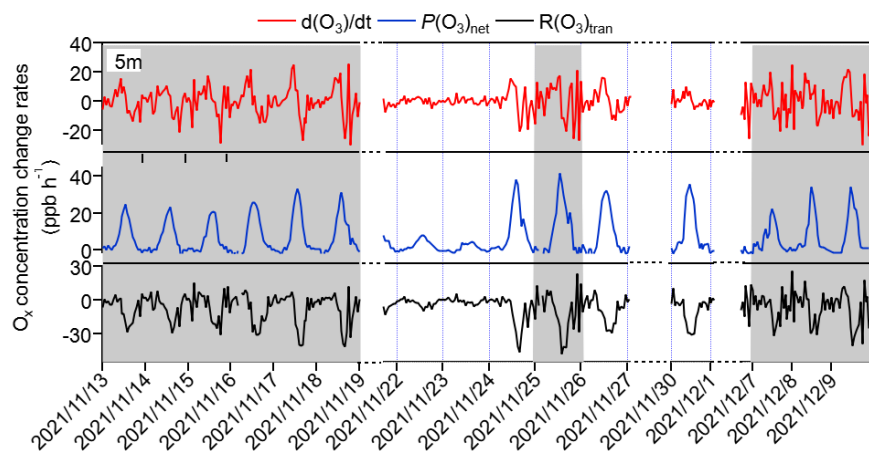
462

463 **Figure 4. Time series of O_3 contributions from local photochemical production and physical**
464 **transport.**

465

470
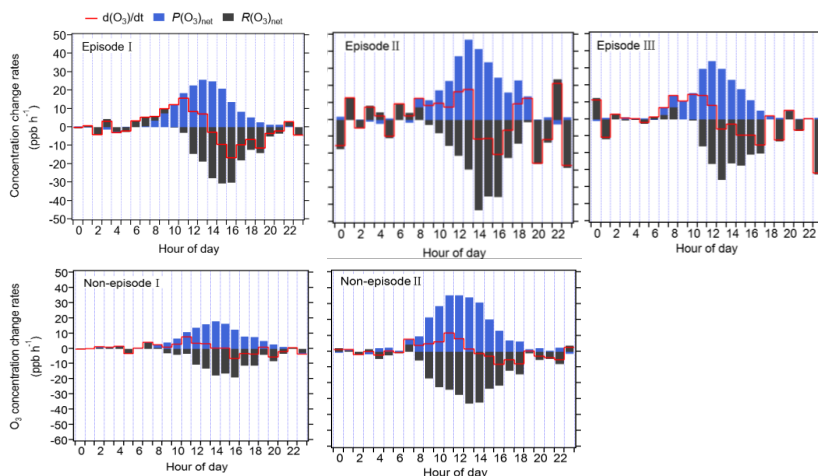
474 **Figure 5. Diurnal variation of the contribution of chemical and physical transport to O_3**
475 **changes on the ground level.**

476   The results shown here indicate that fluctuation of the O_3 concentration change

477   rate (represented as d(O$_3$)/dt) on the ground level was usually small and dominated by
478   the physical processes during nighttime. At around 6:00-7:00, O$_3$ concentrations were
479   increasing for all episodes and non-episodes, mainly attributed to the physical transport,
480   this may be due to the short-term strong vertical turbulence in the early morning due to
481   the expansion of the boundary layer height, which make the residual layer became
482   "leaky" and vertical transport occurred. During this time, the O$_3$ precursors were also
483   transported down from the residue layer and the sun radiation start to increase, O$_3$
484   precursors were then underwent the rapid photochemical reaction and led to the sharp
485   increase of $P(O_3)_{net}$ between 8:00 to 12:00. The $P(O_3)_{net}$ reached a peak at around 11:00-
486   14:00, and started to decrease at around 15:00, which approached zero at around 19:00-
487   20:00. Between 7:00-8:00, $R(O_3)_{tran}>0$ for all episodes and non-episodes, indicating the
488   inflow of O$_3$ from physical transport, the physical transport increase the surface O$_3$
489   concentration by 4.7, 3.9, 2.3, 3.5, and 4.5 ppbv h^{-1} on average for episodes I, II, III,
490   and non-episodes I and II, respectively. From 9:00 to 10:00, $R(O_3)_{tran}>0$ for episodes I,
491   which increase the O$_3$ concentration by 1.5 ppbv h^{-1}, indicating the inflow of O$_3$ from
492   physical transport; on the contrary, $R(O_3)_{tran}<0$ for episodes II and III, and non-episodes
493   I and II, indicating the outflow of O$_3$ from physical transport, which decrease the O$_3$
494   concentration by 3.1, 0.1, 3.0, and 16.9 ppbv h^{-1}, respectively. After 10:00, $R(O_3)_{tran}<0$
495   for all episodes and non-episodes, indicating the outflow of O$_3$ from the observation
496   sites, this may be due to the accumulation of the photochemically formed O$_3$ increases
497   the O$_3$ concentration at the observation site, thus diffuses to upward directions or the
498   surrounding areas.

499   In conclusion, the observed daytime O$_3$ concentration change during all episodes
500   and non-episodes was influenced by both photochemical production and physical
501   transport. In the early morning, O$_3$ concentrations increase can be attributed to
502   photochemical reaction, physical process, and may also be the reduced NO titration
503   effects as the boundary layer height increases. At around noon time, the O$_3$
504   concentration became stable, suggests that the photochemical reaction competed
505   against physical transport and jointly affect O$_3$ concentration change. In the afternoon,
506   the O$_3$ concentration decreases due to the diffuse of photochemically formed O$_3$ from
507   the observation site to upward directions or the surrounding areas. Our findings suggest
508   that local photochemical reaction dominates O$_3$ pollution. For example, O$_3$ pollution
509   episodes recorded during the observation period manifest under specific conditions: ①

510   high photochemical O_3 production (i.e., episode II); ② moderate photochemical O_3

511   productions coupled with O_3 accumulation under stable weather conditions (i.e.,

512   episodes I and III). In contrast, non-episodes observed during the observation period

513   occur under different conditions: ① low levels of photochemical O_3 production (i.e.,

514   non-episodes I); ② elevated photochemical O_3 production, with O_3 diffuse to

515   surrounding areas under favorable diffusion conditions (i.e., non-episodes II).

3.2.2   The model performance

517   In order to test the simulation ability of MCM model for $P(O_3)_{net}$, we compared

518   the measured and modelled $P(O_3)_{net}$ at 5 m ground level, as depicted in Fig. S2. The

519   measured $P(O_3)_{net}$ exhibited close alignment with the values during episodes I and III,

520   yet displayed discernible variations during episode II, non-episode I, and non-episode

521   II. Assessment metrics including IOA, NMB and NME were computed based on the

522   observed and modelled $P(O_3)_{net}$ at 5 m level over the whole measurement period as

523   described in Sect. 2.3.3. Results revealed an IOA range between 0.87 (25th percentile)

524   and 0.90 (75th percentile) for the measured and modelled $P(O_3)_{net}$ across the

525   measurement period, indicating the acceptable performance of the MCM model

526   simulation (a higher IOA value signifies a stronger agreement between simulated and

527   observed values). We also compared the measured and modelled O_3 concentrations at

528   different heights (as shown in Fig. S3). Notably, during daytime, the modelled O_3

529   concentrations generally exhibited higher values than the measured O_3 concentrations.

530   However, during nighttime, the modelled O_3 concentrations closely matched the

531   measured values at lower heights (i.e., 5 m, 40 m, and 70 m), but were mostly higher

532   than the measured values at higher heights (i.e., 120 m, 220 m, and 335 m), these

533   phenomena may be primarily attributed to uncertainties in the assumed physical

534   processes (such as vertical and horizontal transport) in the modelling, the effect of

535   which was set as a constant dilution factor of 1/43200 s^{-1} during the whole modelling

536   period. Further investigations revealed an IOA range between 0.80 (25th percentile) and

537   0.82 (75th percentile) for the measured and modelled O_3 concentrations at 5 m ground

538   level, which lies in between the IOA result for the modelled and observed O_3

539   concentrations in previous studies, which range between 0.68 and 0.89 (Wang et al.,

540   2018), signifying the modelling results for O_3 concentrations here are acceptable. The

541   calculated NMB and NME using the modelled and observed $P(O_3)_{net}$ at 5 m ground

542   level during the whole measurement period ranged from -0.42 (25th percentile) to -0.31

543   (75th percentile) and -0.42 (25th percentile) to 0.54 (75th percentile), respectively.

544   The mean diel variation of measured and modelled $P(O_3)_{net}$ during different

545   episodes and non-episodes are shown in Fig. 6a-e. The maximum daily $P(O_3)_{net}$ values

546   were 29.3, 47.2, and 34.2 ppbv h^{-1} for episodes I, II, and III, and 17.9 and 35.5 non-

547   episodes I and II, respectively. These maximum daily $P(O_3)_{net}$ values were similar or

548   lower than that measured in the urban area of Houston in the United States (40-50 and

549   100 ppbv h^{-1} in autumn and spring, respectively) (Baier et al., 2015; Ren et al., 2013),

550   and in Indiana in the United States (~ 30 ppbv h^{-1} in spring) (Sklaveniti et al., 2018),

551   but higher than that measured at the Wakayama Forest Research Station in a remote

552   area of Japan (10.5 ppbv h^{-1} in summer, Sadanaga et al., 2017) and in an urban area of

553   Pennsyvania in the United States (~ 8 ppbv h^{-1} in summer) (Cazorla and Brune, 2020).

554   The averaged diel profiles of the measured and simulated $P(O_3)_{net}$ have large standard

555   deviations (as depicted in Table 1), representing their day-to-day variation throughout

556   the campaign. The results shown in Fig. 6a-e indicate that the measured $P(O_3)_{net}$ were

557   mostly higher than the modelled $P(O_3)_{net}$. Previous studies have highlighted the

558   presence of missing RO_2 under high NO conditions, contributing significantly to

559   substantial disparities between calculated $P(O_3)_{net}$ derived from measured and modelled

560   RO_2 concentrations (Whalley et al., 2018, 2021; Tan et al., 2017, 2018). To delve

561   deeper, we further investigated the relationship between the average daily disparities of

562   measured and modelled $P(O_3)_{net}$ ($\Delta P(O_3)_{net}$) and the average daytime NO

563   concentrations during different episodes and non-episodes, as depicted in Fig. 6f. The

564   observed elevated $\Delta P(O_3)_{net}$ at higher NO concentrations aligns with findings from

565   previous studies, which suggest that multiple factors could contribute to these outcomes.

566   For example, the reaction of OH with unknown VOCs (Tan et al., 2017), the lack of the

567   correction for the decomposition of $CH_3O_2NO_2$ or the missing RO_2 production from the

568   photolysis $ClNO_2$ (Whalley et al., 2018; Tan et al., 2017), and the underestimation of

569   OVOCs photolysis (Wang et al., 2022) in modelling approach, may result in the

570   underestimation of RO_2, thus underestimate the modelled $P(O_3)_{net}$ and the NOx-limited

571   regime. Nonetheless, the derived IOA, NMB, and NME values from the modelled and

572   observed $P(O_3)_{net}$ at 5 m ground, as previously outlined, indicate that the model

573   proficiently reproduces the genuine $P(O_3)_{net}$ at the observation site. Consequently, these

574   results give us confidence to explore the vertical and temporal variations of $P(O_3)_{net}$

575 and O_3 formation sensitivities utilizing the outcomes from the modelling approach.

576 However, it is important to acknowledge and discuss the potential biases caused by the

577 modelling methodology in this study.
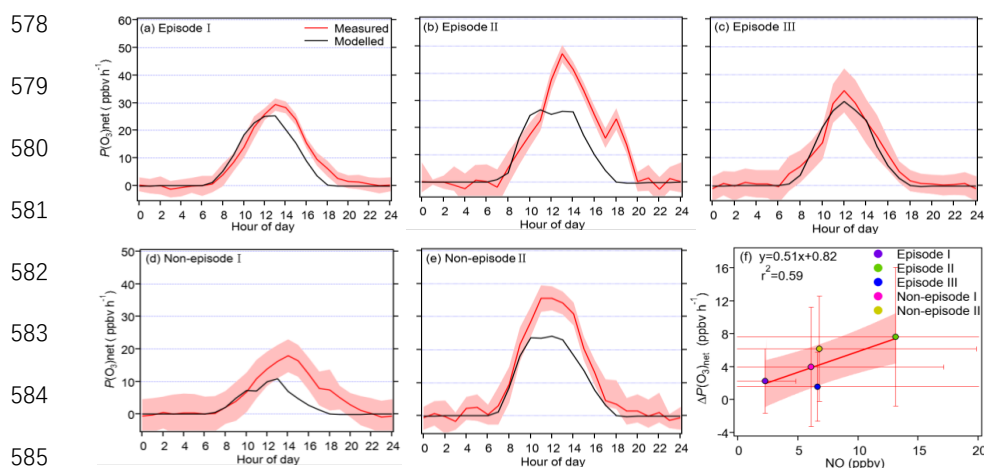
Figure 6. (a-e) diurnal variations of the measured and modelled $P(O_3)_{net}$ during the observation period, and (f) the relationship between the average daily differences of measured and modelled $P(O_3)_{net}$ ($\Delta P(O_3)_{net}$) and the average daytime NO concentrations during different episodes and non-episodes.

3.2.3 Vertical and temporal variability of $P(O_3)_{net}$ budget

591 The detailed $P(O_3)_{net}$ budget at different heights during the observation period from the

592 modelling results are shown in Fig. 7. We saw that at different heights, or at different

593 episodes and non-episodes, the contributions of different reaction pathways to $P(O_3)$

594 were almost the same, with HO_2+NO as the major O_3 production pathway, followed by

595 CH_3O_2+NO and other RO_2+NO, where other RO_2+NO is defined as all RO_2 except

596 CH_3O_2, these results are similar with previous studies (Liu et al., 2021; Liu et al., 2022).

597 The major O_3 destruction pathway was $OH+NO_2$ (loss of OH radicals), followed by net

598 RO_2+NO_2 (form peroxyacetyl nitrate, commonly called PAN species) and O_3

599 photolysis, while the other O_3 destruction pathways, including O_3+OH, O_3+HO_2,

600 $C_5H_8+O_3$, $C_3H_6+O_3$, and $C_2H_4+O_3$ together contributed a negligible O_3 destruction. All

601 these $P(O_3)$ and $D(O_3)$ reaction pathways happened between 6:00-18:00 LT, and

602 showed a strong diurnal variation, which increased sharply between at 6:00-11:00 LT

603 in the morning, reached a peak between 11:00 and 14:00 LT, and decreased quickly

604 after 14:00 LT. These phenomena were in accordance with the concentration changes

605 of the major oxidants (i.e., OH, O_3, and NO_3), as shown in Fig. S4. OH radicals and O_3

606 concentrations increased significantly in the morning and reached a peak at around

607 noon time, and decreased sharply in the afternoon.

608
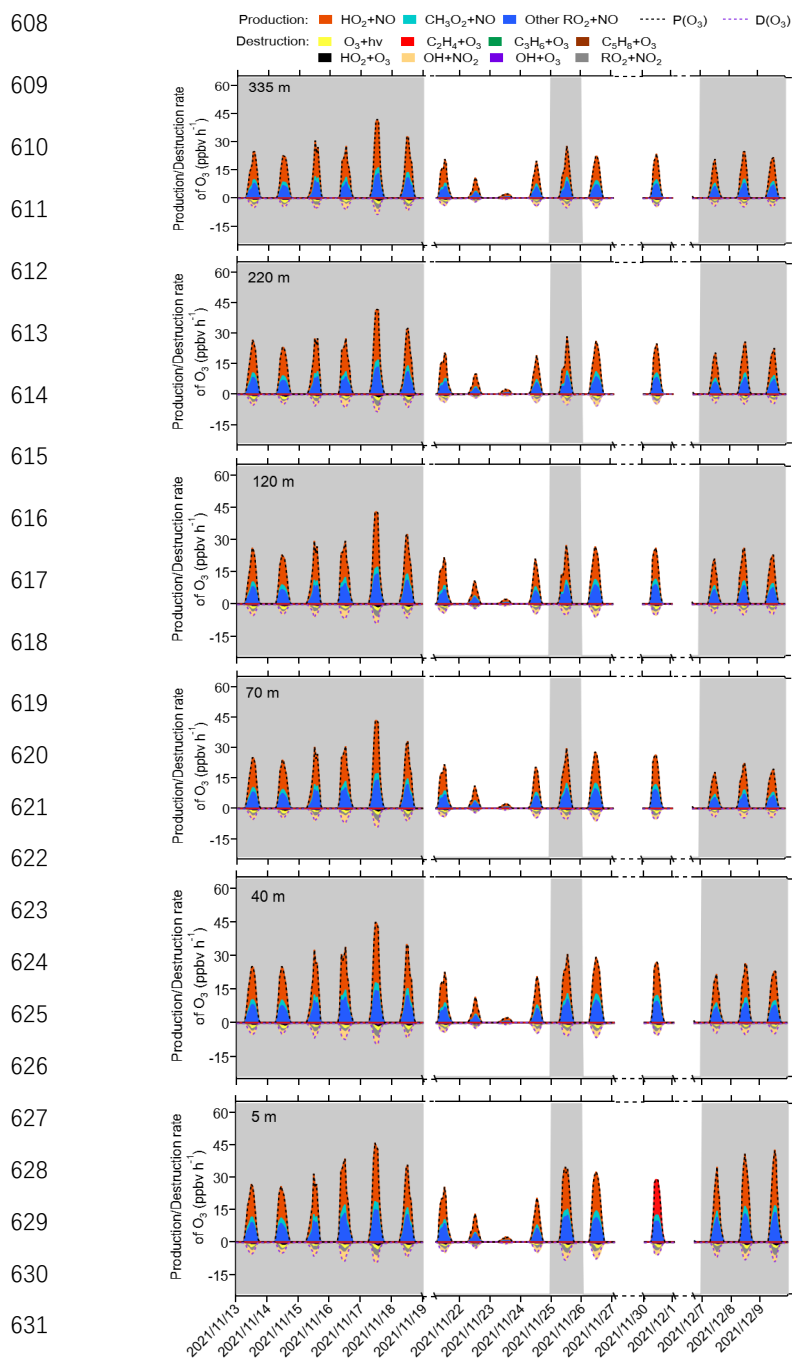
632 **Figure 7:Time series of model-simulated O_3 production and destruction rates during 13**
633 **November and 9 December 2021, at different heights at SZMGT, the gray columns show the**
634 **typical ozone episodes that occurred.**

635   The diurnal changes in the concentrations of different reaction pathways to $P(O_3)$
636 and $D(O_3)$ at 5 m ground level during different episodes and non-episodes are depicted
637 in Fig. S5. We note that the maximum total $P(O_3)$ resulting from diel variations at 5 m
638 ground level for episode I, II, and III were 32.0, 34.9, and 38.3 ppbv h^{-1}, respectively.
639 These values were consistently higher than the maximum total $P(O_3)$ observed for non-
640 episodes I and II, which were 15.6 and 30.7 ppbv h^{-1}, respectively. However, as $P(O_3)_{net}$
641 was determined by both $P(O_3)$ and $D(O_3)$, the maximum total $D(O_3)$ values resulting
642 from diel variations during episodes I, II, III, and non-episode I, II, were 5.0, 5.7, 5.1,
643 2.4, and 5.3 ppbv h^{-1}, respectively. Consequently, the modelled $P(O_3)_{net}$ during episodes
644 not exhibiting a statistically difference with that during non-episodes, as shown in Fig.
645 S5, which is in accordance with the measured $P(O_3)_{net}$ as depicted in Sect. 3.1.1.

646   The diurnal variation of $P(O_3)_{net}$ during different episodes and non-episodes
647 obtained by MCM modelling at different heights are shown in Fig. 8. We saw that the
648 $P(O_3)_{net}$ all showed a decrease trend with the increase of the measurement height during
649 different episodes and non-episodes, but the $P(O_3)_{net}$ variation along with the
650 measurement height differs for different episodes and non-episodes. For example, the
651 decrement of the averaged $P(O_3)_{net}$ during 6:00-18:00 from 5 m to 335 m are 1.5 and
652 0.6 ppbv h^{-1} for episode I and non-episode I, respectively, which are relatively smaller
653 than that during episode II, episode III, and non-episode II, which are 5.3, 5.4, and 4.0
654 ppbv h^{-1}, respectively. To explore the reason, we plotted the differences of calculated
655 OH reactivities at 5 m and 335 m of different VOCs groups (marked as ΔOH reactivity)
656 as a function of the $P(O_3)_{net}$ change at 5 m and 335 m (marked as $\Delta P(O_3)_{net}$), including
657 nonmethane hydrocarbons (NMHC), anthropogenic volatile organic compounds
658 (AVOC), biogenic volatile organic compounds (BVOC), and oxygenated volatile
659 organic compounds (OVOC) (as shown in Fig.8f). We found that OH reactivities of
660 AVOC and OVOC have the highest correlation coefficients (R^2) with the $\Delta P(O_3)_{net}$,
661 which are 0.85 and 0.67, respectively, indicates their predominant influence to the
662 decrement of $P(O_3)_{net}$ from 5 m to 335 m. However, the OH reactivity change from 5
663 m to 335 m of different groups are pretty different, therefore, we further explored O_3
664 formation sensitivity to its different precursors and precursor groups.
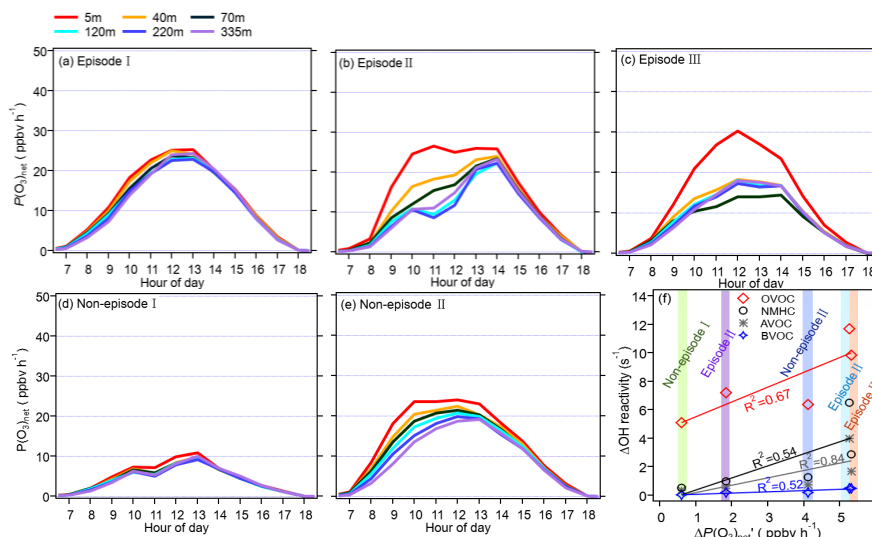
Figure 8: (a-e) Diurnal variation of vertical profile of the model-simulated $P(O_3)_{net}$ during different episodes and non-episodes from 13 November to 9 December 2021, and (f) the relationship between the average daytime differences of modelled $P(O_3)_{net}$ (denoted as $\Delta P(O_3)_{net}$), and OH reactivity of different precursor groups at 5 m and 335 m (denoted as ΔOH reactivity).

3.2.4 Vertical distributions of O₃ formation regime

To investigate the reason for the variable $P(O_3)_{net}$ distribution at varying heights, the sensitivity of O₃ formation to different O₃ precursors or precursor groups, including NMHC, AVOC, BVOC, OVOC, CO, and NOx, were clarified by calculating their RIRs during different episodes and non-episodes, as shown in Fig. 9.

695
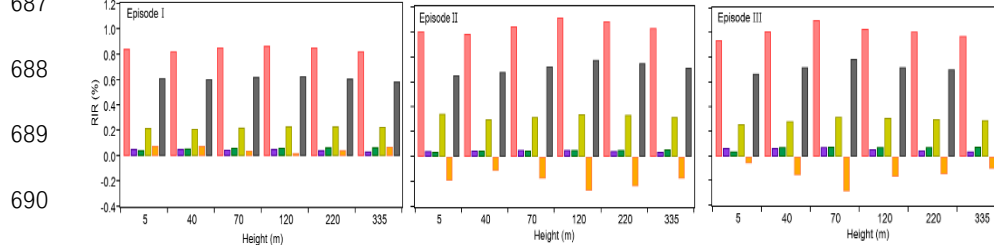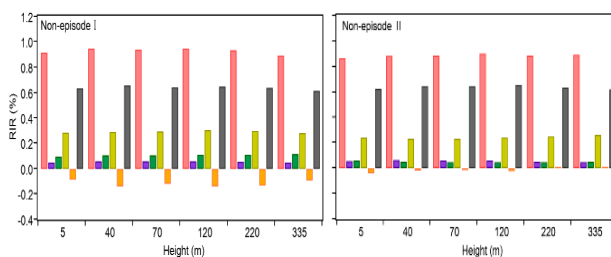
Figure 9: RIR values for O₃-precursor or precursor groups at different heights during different classified episodes.

As illustrated in Fig. 9, for a specific episode or non-episode, the RIR values for different O₃-precursors or precursor groups don't have significant variation at different heights, indicates the similar photochemical O₃ formation regime. However, for different episodes or non-episodes, the O₃ formation regimes are different. The O₃ formation located in transition regime and more sensitive to VOCs emissions during O₃ polluted episode I. Conversely, it is located in VOCs sensitive regime during O₃ polluted episodes II and III, and non-episodes I and II. This outcome is in accordance with previous studies that photochemical O₃ formation in the PRD region is likely VOC-limited or mixed-limited (Hong et al., 2022; Lu et al., 2018). The results shown here indicate the complexity of O₃ mitigation at the observation site. For example, during polluted episode I, both reduce VOCs and NOx can mitigate photochemical O₃ formation, but during the other O₃ polluted episodes and non-episodes, reduce VOCs can effectively alleviate photochemical O₃ formation, while the reduction of NOx might aggravate photochemical O₃ formation. Still, during all episodes and non-episodes, O₃ formation are most sensitive to AVOC (RIR: 0.83-1.12), followed by OVOC (RIR: 0.59-0.79) at different heights, indicates the urgent needs to reduce AVOC and OVOC emissions to mitigate O₃ pollution in this area.

The RIR tests for different episodes and non-episodes at different hours of the local day time are shown in Supplement (Fig. S6). Results show that the diurnal changes of RIR values for different episodes and non-episodes are quite similar. In the morning time, the RIR values for different VOC groups, including AVOC, BVOC, OVOC, and CO are usually higher than that for NOx, but gradually decrease in the following hours of the day until 16:00 LT, which were then increase and reach a peak at 18:00 LT, but the RIR values at this peak are lower than those at 8:00 LT in the morning. For the RIR values for NOx, they are usually around zero or below zero, and then gradually increase at around 16:00 LT and then reaches a peak at 18:00 LT, this indicates that the photochemical O₃ formation regime changes during the daytime, which located in the VOC-limited regime in the morning and changes to transition regime but more sensitive to NOx in the afternoon at around 16:00 LT. The diurnal variations of the RIRs of different O₃ precursor or precursor groups could provide us more detailed information

728 to diagnose the dominating factor that influence the photochemical formation of O_3 at

729 different time of a day.

730 Through the sensitivity study, we note that NOx would not be the limiting factor

731 that effect $P(O_3)_{net}$, thus the ROx radicals cycle reactions involved NOx should

732 occurred efficiently, such as $RO_2+NO \rightarrow HO_2$ and $HO_2+NO \rightarrow OH$. Meanwhile, the

733 reactions that not involved NOx should be the limiting steps of ROx radicals cycling,

734 such as $OH+VOCs \rightarrow RO_2$. As the photochemical O_3 formation were most sensitive to

735 AVOC, OVOC and NMHC groups, hence, we should take the priority to reduce AVOC

736 and OVOC to mitigate O_3 pollution in PRD area in China.

737 **4. Conclusions**

738 We carried out a field observation campaign to investigate the vertical temporal

739 variability of near-surface ozone production mechanism in an urban area in Pearl River

740 Delta (PRD) in China, by using a newly built vertical observation system and the

741 observation-based model coupled to the Master Chemical Mechanism (OBM-MCM)

742 v3.3.1. In total 3 O_3 pollution episodes and 2 non-episodes happened during the

743 observation period. In order to check the modelling performance for O_3 production rates

744 and sensitivity, and the possible reason for O_3 pollution episodes at 5 m ground level,

745 a net photochemical ozone production rate (NPOPR, $P(O_3)_{net}$) detection system based

746 on the current dual-channel reaction chamber technique was employed to directly

747 measure $P(O_3)_{net}$ at 5 m ground-level.

748 The vertical profiles of averaged concentrations of various pollutants exhibit similar

749 trends during both episodes and non-episodes. The O_3, NOx, and Ox concentrations

750 show minimal vertical gradient during daytime due to the rapid vertical mixing effects,

751 but there are distinct vertical gradients during nighttime owing to the stability of the

752 nocturnal residual layer. Higher concentrations of O_3 and Ox were found at higher

753 heights, while higher NO and NOx concentrations mainly occurred at ground level.

754 Given that NOx has a significant titration effect on ozone, the lower O_3 concentration

755 at ground level may be attributed to the increase in NOx concentration due to a more

756 pronounced NO titration effect, besides the dry deposition near the ground. However,

757 the TVOC and their OFP showed variable trends with the increased height for daytime

758 and nighttime during episodes and non-episodes. Total OFP was highest at 5 m ground

759 level and exhibited higher levels during episodes compared to non-episode periods. The

760 OFP was primarily attributed to OVOCs at different altitudes throughout both episodes
761 and non-episodes.

762   The mean concentrations of O_3 precursors, including CO, NO, NO_2, and TVOC,
763 were not statistically different between episodes and non-episodes. By combining the
764 observed O_3 concentrations change and the measured $P(O_3)_{net}$ at 5 m ground level, we
765 found that the O_3 pollution episodes were jointly influenced by both photochemical
766 production and physical transport, with local photochemical reactions play a dominate
767 role. O_3 pollution episodes recorded during the observation period manifest under
768 specific conditions: ① high photochemical O_3 productions; ② moderate photochemical
769 O_3 productions coupled with O_3 accumulation under stable weather conditions. The
770 index of agreement (IOA) ranged from 0.87 (25th percentile) to 0.90 (75th percentile)
771 for the measured and modelled $P(O_3)_{net}$ across the measurement period, indicated the
772 rationality to investigate the vertical and temporal variability of O_3 formation
773 mechanism using modelling results. However, the measured $P(O_3)_{net}$ were generally
774 higher than the modelled $P(O_3)_{net}$, the differences of measured and modelled $P(O_3)_{net}$
775 ($\Delta P(O_3)_{net}$) are correlated with the NO concentrations. Base on previous studies, this
776 phenomenon could potentially be attributed to the underestimation of RO_2 at high NO
777 conditions, arising from inadequate knowledge concerning photochemical reaction
778 mechanisms. Therefore, the potential biases caused by the modelling methodology
779 were acknowledged and discussed.

780   From the modelling results, the contribution of different reaction pathways to $P(O_3)$
781 were almost the same at varying heights during episodes and non-episodes, with
782 HO_2+NO as the major O_3 production pathway, followed by other RO_2+NO (all RO_2
783 except CH_3O_2) and CH_3O_2+NO. The major O_3 destruction pathway was OH+NO_2 (loss
784 of OH radicals), followed by net RO_2+NO_2 (form peroxyacetyl nitrate) and O_3
785 photolysis, while the other O_3 destruction pathways, including O_3+OH, O_3+HO_2,
786 C_5H_8+O_3, C_3H_6+O_3, and C_2H_4+O_3 together contributed a negligible O_3 destruction.
787 However, $P(O_3)_{net}$ showed a decrease trend with the increase of height during different
788 episodes and non-episodes, which was found mainly due to the decrease of O_3 precursor
789 anthropogenic organic compounds (AVOC) and oxygenated volatile organic
790 compounds (OVOC) groups. We find that the modelling biases were correlated with
791 NO concentrations and VOCs categories, which impact $P(O_3)_{net}$ through the regulation

792   of the RO_2 radicals' budget. The maximum estimated error of modelled $P(O_3)_{net}$ ranged

793   from 22-45 % during different episodes and non-episodes. Therefore, the $P(O_3)_{net}$

794   variation along with the measurement height might be even larger than our initial

795   assessment.

796   Similar photochemical O_3 formation regimes were observed at different heights for

797   a specific episode or non-episode, yet they varied between different episodes or non-

798   episodes. The O_3 formations were located in transition regime and more sensitive to

799   VOCs emissions during O_3 polluted episode I; whereas located in VOCs sensitive

800   regime during O_3 polluted episodes II and III, and non-episodes I and II. Further

801   analysis revealed a daytime shift in photochemical O_3 formation regime, which located

802   in the VOC-limited regime in the morning and changes to transition regime but more

803   sensitive to NOx at around 16:00 LT in the afternoon. However, the underestimation of

804   RO_2 radicals in the modelling, especially at lower heights with higher NO

805   concentrations, could resulted in an overestimate of the VOCs-limited regime. This

806   study heights the need for more precise analysis using the direct measurement

807   techniques in future studies. Still, throughout all episodes and non-episodes, O_3

808   formation are most sensitive to AVOC, followed by OVOC at various heights,

809   emphasizing the urgent needs to reduce emissions of these compounds to mitigate O_3

810   pollution in this area.

811   This is the first measurement report of the vertical temporal of O_3 formation

812   mechanisms near the ground surface. Together with the deliberation of the possible bias

813   on the vertical temporal profile of O_3 formation rate and sensitivity using modelling

814   study, this study provides the critical foundational insights. The research findings

815   provide us in-depth understanding of near-ground vertical variability of O_3 formation

816   mechanism, which benefit us to formulate proper ozone control strategies in PRD area

817   in China.

818   *Data availability.* Data related to this article are available online *at*

819   https://zenodo.org/records/10473104.

820   *Author contributions.* BY, JZ, XBL, and MS designed the experiment, YXH and JZ

821   performed the $P(O_3)_{net}$ measurement, BY and XBL built the vertical observation system

822   based on SZMGT. JZ, CZ, AL, BY, JPZ, YXH, YW, XBL, XJH, XS, YC, SY, SY,

823   YW, JPQ collected and analysed the data. JZ wrote the manuscript, all authors revised

824   the manuscript.

825   *Competing interests.* The authors declare that they have no known competing interests.

826   *Acknowledgements.* This study was funded by the Key-Area Research and
827   Development Program of Guangdong Province (grant no. 2020B1111360003), the
828   National Natural Science Foundation of China (No. 42305096), and the Natural Science
829   Foundation of Guangdong Province (grant no. 2020A1515110526).

830   **References**

831   Anenberg, S. C., Schwartz, J., Shindell, D., Amann, M., Faluvegi, G., Klimont, Z., Janssens-
832   Maenhout, G., Pozzoli, L., Van Dingenen, R., Vignati, E., Emberson, L., Muller, N. Z.,
833   West, J. J., Williams, M., Demkine, V., Hicks, W. K., Kuylenstierna, J., Raes, F., and
834   Ramanathan, V.: Global air quality and health co-benefits of mitigating near-term climate
835   change through methane and black carbon emission controls, Environ. Health. Perspect.,
836   120, 831-839, 10.1289/ehp.1104301, 2012.
837   Baier, B. C., Brune, W. H., Lefer, B. L., Miller, D. O., and Martins, D. K.: Direct ozone
838   production rate measurements and their use in assessing ozone source and receptor regions
839   for Houston in 2013, Atmos. Environ., 114, 83-91, 10.1016/j.atmosenv.2015.05.033, 2015.
840   Benish, S. E., He, H., Ren, X., Roberts, S. J., Salawitch, R. J., Li, Z., Wang, F., Wang, Y.,
841   Zhang, F., Shao, M., Lu, S., and Dickerson, R. R.: Measurement report: Aircraft
842   observations of ozone, nitrogen oxides, and volatile organic compounds over Hebei
843   Province, China, Atmos. Chem. Phys., 20, 14523-14545, 10.5194/acp-20-14523-2020,
844   2020.
845   Cazorla, M. and Brune, W. H.: Measurement of ozone production sensor, Atmos. Meas. Tech.,
846   3, 545-555, 10.5194/amt-3-545-2010, 2010.
847   Fiore, A. M., Dentener, F. J., Wild, O., Cuvelier, C., Schultz, M. G., Hess, P., Textor, C., Schulz,
848   M., Doherty, R. M., Horowitz, L. W., MacKenzie, I. A., Sanderson, M. G., Shindell, D. T.,
849   Stevenson, D. S., Szopa, S., Van Dingenen, R., Zeng, G., Atherton, C., Bergmann, D., Bey,
850   I., Carmichael, G., Collins, W. J., Duncan, B. N., Faluvegi, G., Folberth, G., Gauss, M.,
851   Gong, S., Hauglustaine, D., Holloway, T., Isaksen, I. S. A., Jacob, D. J., Jonson, J. E.,
852   Kaminski, J. W., Keating, T. J., Lupu, A., Marmer, E., Montanaro, V., Park, R. J., Pitari,
853   G., Pringle, K. J., Pyle, J. A., Schroeder, S., Vivanco, M. G., Wind, P., Wojcik, G., Wu, S.,
854   and Zuber, A.: Multimodel estimates of intercontinental source-receptor relationships for
855   ozone pollution, J. Geophys. Res., 114, 10.1029/2008jd010816, 2009.
856   Geng, C., Wang, J., Yin, B., Zhao, R., Li, P., Yang, W., Xiao, Z., Li, S., Li, K., and Bai, Z.:
857   Vertical distribution of volatile organic compounds conducted by tethered balloon in the
858   Beijing-Tianjin-Hebei region of China, J. Environ. Sci., 95, 121-129,
859   10.1016/j.jes.2020.03.026, 2020.
860   Hao, Y., Zhou, J., Zhou, J. P., Wang, Y., Yang, S., Huangfu, Y., Li, X. B., Zhang, C., Liu, A.,
861   Wu, Y., Zhou, Y., Yang, S., Peng, Y., Qi, J., He, X., Song, X., Chen, Y., Yuan, B., and
862   Shao, M.: Measuring and modeling investigation of the net photochemical ozone
863   production rate via an improved dual-channel reaction chamber technique, Atmos. Chem.
864   Phys., 23, 9891-9910, 10.5194/acp-23-9891-2023, 2023.
865   Hong, Q., Zhu, L., Xing, C., Hu, Q., Lin, H., Zhang, C., Zhao, C., Liu, T., Su, W., and Liu, C.:
866   Inferring vertical variability and diurnal evolution of O_3 formation sensitivity based on the
867   vertical distribution of summertime HCHO and NO_2 in Guangzhou, China, Sci. Total
868   Environ., 827, 10.1016/j.scitotenv.2022.154045, 2022.
869   Jenkin, M. E., Young, J. C., and Rickard, A. R.: The MCM v3.3.1 degradation scheme for
870   isoprene, Atmos. Chem. Phys., 15, 11433-11459, 10.5194/acp-15-11433-2015, 2015.
871   Klein, A., Ravetta, F., Thomas, J. L., Ancellet, G., Augustin, P., Wilson, R., Dieudonné, E.,

872   Fourmentin, M., Delbarre, H., and Pelon, J.: Influence of vertical mixing and nighttime
873   transport on surface ozone variability in the morning in Paris and the surrounding region,
874   Atmos. Environ., 197, 92-102, 10.1016/j.atmosenv.2018.10.009, 2019.
875   Li, X.-B., Yuan, B., Wang, S., Wang, C., Lan, J., Liu, Z., Song, Y., He, X., Huangfu, Y., Pei,
876   C., Cheng, P., Yang, S., Qi, J., Wu, C., Huang, S., You, Y., Chang, M., Zheng, H., Yang,
877   W., Wang, X., and Shao, M.: Variations and sources of volatile organic compounds (VOCs)
878   in urban region: insights from measurements on a tall tower, Atmos. Chem. Phys., 22,
879   10567-10587, 10.5194/acp-22-10567-2022, 2022b.
880   Li, X.-B., Zhang, C., Liu, A., Yuan, B., Yang, H., Liu, C., Wang, S., Huangfu, Y., Qi, J., Liu,
881   Z., He, X., Song, X., Chen, Y., Peng, Y., Zhang, X., Zheng, E., Yang, L., Yang, Q., Qin,
882   G., Zhou, J., and Shao, M.: Assessment of long tubing in measuring atmospheric trace gases:
883   applications on tall towers, Environ. Sci.: Atmos., 3, 506-520, 10.1039/d2ea00110a, 2023.
884   Li, X., Qin, M., Li, L., Gong, K., Shen, H., Li, J., and Hu, J.: Examining the implications of
885   photochemical indicators for O_3–NOx–VOC sensitivity and control strategies: a case study
886   in the Yangtze River Delta (YRD), China, Atmos. Chem. Phys., 22, 14799-14811,
887   10.5194/acp-22-14799-2022, 2022a.
888   Li, Y., Liu, B., Ye, J., Jia, T., Khuzestani, R. B., Sun, J. Y., Cheng, X., Zheng, Y., Li, X., Wu,
889   C., Xin, J., Wu, Z., Tomoto, M. A., McKinney, K. A., Martin, S. T., Li, Y. J., and Chen,
890   Q.: Unmanned aerial vehicle measurements of volatile organic compounds over a
891   subtropical forest in China and implications for emission heterogeneity, ACS. Earth. Space.
892   Chem., 5, 247-256, 10.1021/acsearthspacechem.0c00271, 2021.
893   Liu, T., Hong, Y., Li, M., Xu, L., Chen, J., Bian, Y., Yang, C., Dan, Y., Zhang, Y., Xue, L.,
894   Zhao, M., Huang, Z., and Wang, H.: Atmospheric oxidation capacity and ozone pollution
895   mechanism in a coastal city of southeastern China: analysis of a typical photochemical
896   episode by an observation-based model, Atmos. Chem. Phys., 22, 2173-2190, 10.5194/acp-
897   22-2173-2022, 2022.
898   Liu, X., Wang, N., Lyu, X., Zeren, Y., Jiang, F., Wang, X., Zou, S., Ling, Z., and Guo, H.:
899   Photochemistry of ozone pollution in autumn in Pearl River Estuary, South China, Sci.
900   Total Environ., 754, 141812, 10.1016/j.scitotenv.2020.141812, 2021.
901   Liu, Z., Zha, F., Wang, Y., Yuan, B., Liu, B., and Tang, G.: Vertical evolution of the
902   concentrations and sources of volatile organic compounds in the lower boundary layer in
903   urban   Beijing   in   summer,   Chemosphere,   332,   138767,
904   10.1016/j.chemosphere.2023.138767, 2023.
905   Lu, X., Hong, J., Zhang, L., Cooper, O. R., Schultz, M. G., Xu, X., Wang, T., Gao, M., Zhao,
906   Y., and Zhang, Y.: Severe surface ozone pollution in China: a global perspective, Environ.
907   Sci. Technol. Lett., 5, 487-494, 10.1021/acs.estlett.8b00366, 2018.
908   Luo, Y., Dou, K., Fan, G., Huang, S., Si, F., Zhou, H., Wang, Y., Pei, C., Tang, F., Yang, D.,
909   Xi, L., Yang, T., Zhang, T., and Liu, W.: Vertical distributions of tropospheric
910   formaldehyde, nitrogen dioxide, ozone and aerosol in southern China by ground-based
911   MAX-DOAS and LIDAR measurements during PRIDE-GBA 2018 campaign, Atmos.
912   Environ., 226, 10.1016/j.atmosenv.2020.117384, 2020a.
913   Luo, Y. P., Fu, J. Y., Li, Q. S., Chan, P. W., and He, Y. C.: Observation of Typhoon Hato based
914   on the 356-m high meteorological gradient tower at Shenzhen, J. Wind. Eng. Ind. Aerodyn.,
915   207, 104408, 10.1016/j.jweia.2020.104408, 2020b.
916   Mao, J., Yan, F., Zheng, L., You, Y., Wang, W., Jia, S., Liao, W., Wang, X., and Chen, W.:
917   Ozone control strategies for local formation- and regional transport-dominant scenarios in
918   a   manufacturing   city   in   southern   China,   Sci.   Total   Environ.,   813,
919   10.1016/j.scitotenv.2021.151883, 2022.
920   Mousavinezhad, S., Choi, Y., Pouyaei, A., Ghahremanloo, M., and Nelson, D. L.: A
921   comprehensive investigation of surface ozone pollution in China, 2015–2019: Separating
922   the contributions from meteorology and precursor emissions, Atmos. Res., 257,
923   10.1016/j.atmosres.2021.105599, 2021.
924   Pan, X., Kanaya, Y., Tanimoto, H., Inomata, S., Wang, Z., Kudo, S., and Uno, I.: Examining
925   the major contributors of ozone pollution in a rural area of the Yangtze River Delta region

926   during harvest season, Atmos. Chem. Phys., 15, 6101–6111, 10.5194/acp-15-6101-2015,
927   2015.
928 Sadanaga, Y., Kawasaki, S., Tanaka, Y., Kajii, Y., and Bandow, H.: New system for measuring
929   the photochemical ozone production rate in the atmosphere, Environ. Sci. Technol., 51,
930   2871-2878, 10.1021/acs.est.6b04639, 2017.
931 Shen, H., Liu, Y., Zhao, M., Li, J., Zhang, Y., Yang, J., Jiang, Y., Chen, T., Chen, M., Huang,
932   X., Li, C., Guo, D., Sun, X., Xue, L., and Wang, W.: Significance of carbonyl compounds
933   to photochemical ozone formation in a coastal city (Shantou) in eastern China, Sci. Total
934   Environ., 764, 10.1016/j.scitotenv.2020.144031, 2021.
935 Sillman, S.: The relation between ozone, NOx and hydrocarbons in urban and polluted rural
936   environments, Atmos. Environ., 33, 1821-1845, 10.1016/S1352-2310(98)00345-8, 1999.
937 Sklaveniti, S., Locoge, N., Stevens, P. S., Wood, E., Kundu, S., and Dusanter, S.: Development
938   of an instrument for direct ozone production rate measurements: measurement reliability
939   and current limitations, Atmos. Meas. Tech., 11, 741-761, 10.5194/amt-11-741-2018, 2018.
940 Steinfeld, J. I.: Atmospheric chemistry and physics: from air pollution to climate change,
941   Environ. Sci. Policy. Sustain. Dev., 40, 26-26, 10.1080/00139157.1999.10544295, 1998.
942 Tan, Z., Lu, K., Jiang, M., Su, R., Wang, H., Lou, S., Fu, Q., Zhai, C., Tan, Q., Yue, D., Chen,
943   D., Wang, Z., Xie, S., Zeng, L., and Zhang, Y.: Daytime atmospheric oxidation capacity in
944   four Chinese megacities during the photochemically polluted season: a case study based on
945   box model simulation, Atmos. Chem. Phys., 19, 3493-3513, 10.5194/acp-19-3493-2019,
946   2019.
947 Tan, Z., Lu, K., Dong, H., Hu, M., Li, X., Liu, Y., Lu, S., Shao, M., Su, R., Wang, H., Wu, Y.,
948   Wahner, A., and Zhang, Y.: Explicit diagnosis of the local ozone production rate and the
949   ozone-NOx-VOC sensitivities, Sci. Bull., 63(16):1067-1076, 10.1016/j.scib.2018.07.001,
950   2018.
951 Tan, Z., Fuchs, H., Lu, K., Hofzumahaus, A., Bohn, B., Broch, S., Dong, H., Gomm, S., Häseler,
952   R., He, L., Holland, F., Li, X., Liu, Y., Lu, S., Rohrer, F., Shao, M., Wang, B., Wang, M.,
953   Wu, Y., Zeng, L., Zhang, Y., Wahner, A., and Zhang, Y.: Radical chemistry at a rural site
954   (Wangdu) in the North China Plain: observation and model calculations of OH, HO_2 and
955   RO_2 radicals, Atmos. Chem. Phys., 17, 663-690, 10.5194/acp-17-663-2017, 2017.
956 Tang, G., Zhu, X., Xin, J., Hu, B., Song, T., Sun, Y., Zhang, J., Wang, L., Cheng, M., Chao,
957   N., Kong, L., Li, X., and Wang, Y.: Modelling study of boundary-layer ozone over northern
958   China - Part I: Ozone budget in summer, Atmos. Res., 187, 128-137,
959   10.1016/j.atmosres.2016.10.017, 2017.
960 Wang, C., Yuan, B., Wu, C., Wang, S., Qi, J., Wang, B., Wang, Z., Hu, W., Chen, W., Ye, C.,
961   Wang, W., Sun, Y., Wang, C., Huang, S., Song, W., Wang, X., Yang, S., Zhang, S., Xu,
962   W., Ma, N., Zhang, Z., Jiang, B., Su, H., Cheng, Y., Wang, X., and Shao, M.: Measurements
963   of higher alkanes using NO+ chemical ionization in PTR-ToF-MS: important contributions
964   of higher alkanes to secondary organic aerosols in China, Atmos. Chem. Phys., 20, 14123–
965   14138, 10.5194/acp-20-14123- 2020, 2020.
966 Wang, N., Lyu, X., Deng, X., Huang, X., Jiang, F., and Ding, A.: Aggravating O_3 pollution due
967   to NOx emission control in eastern China, Sci. Total Environ., 677, 732-744,
968   10.1016/j.scitotenv.2019.04.388, 2019.
969 Wang, W., Yuan, B., Peng, Y., Su, H., Cheng, Y., Yang, S., Wu, C., Qi, J., Bao, F., Huangfu,
970   Y., Wang, C., Ye, C., Wang, Z., Wang, B., Wang, X., Song, W., Hu, W., Cheng, P., Zhu,
971   M., Zheng, J., and Shao, M.: Direct observations indicate photodegradable oxygenated
972   volatile organic compounds (OVOCs) as larger contributors to radicals and ozone
973   production in the atmosphere, Atmos. Chem. Phys., 22, 4117-4128, 10.5194/acp-22-4117-
974   2022, 2022.
975 Wang, X., Zhang, T., Xiang, Y., Lv, L., Fan, G., and Ou, J.: Investigation of atmospheric ozone
976   during summer and autumn in Guangdong Province with a lidar network, Sci. Total
977   Environ., 751, 10.1016/j.scitotenv.2020.141740, 2021.
978 Wang, Y., Guo, H., Zou, S., Lyu, X., Ling, Z., Cheng, H., and Zeren, Y.: Surface O_3
979   photochemistry over the South China Sea: Application of a near-explicit chemical

980   mechanism box model, Environ. Pollut., 234, 155-166, 10.1016/j.envpol.2017.11.001,
981   2018.
982 Whalley, L. K., Stone, D., Dunmore, R., Hamilton, J., Hopkins, J. R., Lee, J. D., Lewis, A. C.,
983   Williams, P., Kleffmann, J., Laufs, S., Woodward-Massey, R., and Heard, D. E.:
984   Understanding in situ ozone production in the summertime through radical observations
985   and modelling studies during the Clean air for London project (ClearfLo), Atmos. Chem.
986   Phys., 18, 2547-2571, 10.5194/acp-18-2547-2018, 2018.
987 Whalley, L. K., Slater, E. J., Woodward-Massey, R., Ye, C., Lee, J. D., Squires, F., Hopkins, J.
988   R., Dunmore, R. E., Shaw, M., Hamilton, J. F., Lewis, A. C., Mehra, A., Worrall, S. D.,
989   Bacak, A., Bannan, T. J., Coe, H., Percival, C. J., Ouyang, B., Jones, R. L., Crilley, L. R.,
990   Kramer, L. J., Bloss, W. J., Vu, T., Kotthaus, S., Grimmond, S., Sun, Y., Xu, W., Yue, S.,
991   Ren, L., Acton, W. J. F., Hewitt, C. N., Wang, X., Fu, P., and Heard, D. E.: Evaluating the
992   sensitivity of radical chemistry and ozone formation to ambient VOCs and NOx in Beijing,
993   Atmos. Chem. Phys., 21, 2125-2147, 10.5194/acp-21-2125-2021, 2021.
994 Wolfe, G. M., Marvin, M. R., Roberts, S. J., Travis, K. R., and Liao, J.: The Framework for 0-
995   D Atmospheric Modeling (F0AM) v3.1, Geosci. Model. Dev., 9, 3309-3319, 10.5194/gmd-
996   9-3309-2016, 2016.
997 Wu, C., Wang, C., Wang, S., Wang, W., Yuan, B., Qi, J., Wang, B., Wang, H., Wang, C., Song,
998   W., Wang, X., Hu, W., Lou, S., Ye, C., Peng, Y., Wang, Z., Huangfu, Y., Xie, Y., Zhu, M.,
999   Zheng, J., Wang, X., Jiang, B., Zhang, Z., and Shao, M.: Measurement report: Important
1000   contributions of oxygenated compounds to emissions and chemistry of volatile organic
1001   compounds in urban air, Atmos. Chem. Phys., 20, 14769–14785, 10.5194/acp-20-14769-
1002   2020, 2020.

1003 Xue, L. K., Wang, T., Gao, J., Ding, A. J., Zhou, X. H., Blake, D. R., Wang, X. F., Saunders,
1004   S. M., Fan, S. J., Zuo, H. C., Zhang, Q. Z., and Wang, W. X.: Ground-level ozone in four
1005   Chinese cities: precursors, regional transport and heterogeneous processes, Atmos. Chem.
1006   Phys., 14, 13175-13188, 10.5194/acp-14-13175-2014, 2014.
1007 Yang, W., Chen, H., Wang, W., Wu, J., Li, J., Wang, Z., Zheng, J., and Chen, D.: Modeling
1008   study of ozone source apportionment over the Pearl River Delta in 2015, Environ. Pollut.,
1009   253, 393-402, 10.1016/j.envpol.2019.06.091, 2019.
1010 Yuan, B., Chen, W., Shao, M., Wang, M., Lu, S., Wang, B., Liu, Y., Chang, C.-C., and Wang,
1011   B.: Measurements of ambient hydrocarbons and carbonyls in the Pearl River Delta (PRD),
1012   China, Atmos. Res., 116, 93-104, 10.1016/j.atmosres.2012.03.006, 2012.
1013 Yuan, B., Koss, A. R., Warneke, C., Coggon, M., Sekimoto, K., and de Gouw, J. A.: Proton-
1014   Transfer-Reaction Mass Spectrometry: applications in atmospheric sciences, Chem. Rev.,
1015   117, 13187–13229, 10.1021/acs.chemrev.7b00325, 2017.
1016 Zhang, X., Xu, J., Kang, S., Zhang, Q., and Sun, J.: Chemical characterization and sources of
1017   submicron aerosols in the northeastern Qinghai–Tibet Plateau: insights from high-
1018   resolution mass spectrometry, Atmos. Chem. Phys., 19, 7897-7911, 10.5194/acp-19-7897-
1019   2019, 2019.
1020 Zhang, Y., Zhang, Y., Liu, Z., Bi, S., and Zheng, Y.: Analysis of vertical distribution changes
1021   and influencing factors of tropospheric ozone in China from 2005 to 2020 based on multi-
1022   source data, Int. J. Environ. Res. Public Health, 19, 10.3390/ijerph191912653, 2022.
1023 Zhou, J., Yuan, B., Li, X., and Shao, M.: Measurement and modelling results of O_3 and its
1024   precursors [Data set]. Zenodo. 10.5281/zenodo.7854639, 2023.
1025 Zhu, J., Wang, S., Wang, H., Jing, S., Lou, S., Saiz-Lopez, A., and Zhou, B.: Observationally
1026   constrained modeling of atmospheric oxidation capacity and photochemical reactivity in
1027   Shanghai, China, Atmos. Chem. Phys., 20, 1217-1232, 10.5194/acp-20-1217-2020, 2020a.

1028

1029